Statistical Analysis of the Surface Roughness on Aircraft Icing

Denis Sotomayor-Zakharov, Emmanuel Radenac, Mariachiara Gallia, Alberto Guardone, Inken Knop

Statistical analysis of the surface roughness on aircraft icing

Denis Sotomayor-Zakharov*
Technical University of Braunschweig, Braunschweig, Lower Saxony, 38106, Germany

Emmanuel Radenac†
ONERA/DMPE, University of Toulouse, F-31055 Toulouse, France

Mariachiara Gallia‡ and Alberto Guardone §
Polytechnic University of Milan, Milan, 20156, Italy

Inken Knop¶
Technical University of Braunschweig, Braunschweig, Lower Saxony, 38106, Germany

A statistical analysis of the surface roughness is performed on experimentally obtained ice shapes on an asymmetrical airfoil at $Re_c \approx 2 \cdot 10^6$. The ice shapes were generated in the Icing Wind Tunnel of the Technical University of Braunschweig under Appendix C and O conditions of the EASA airplane certification standards as part of the ICE GENESIS project. The photogrammetry method is used for the digitization of the experimental ice shapes, while statistical parameters such as the mean ice shape and the local root mean square (RMS) of the ice geometry are extracted using a traditional surface projection method, as well as a self-organizing maps (SOM) approach. Results show the evolution of the statistical parameters over time and the influence of the freestream static temperature on these parameters. A comparison between the experimental values of the local RMS of the ice geometry and a correlation for roughness prediction is presented, showing a good match with the original formulation of the correlation for cases under Appendix C conditions while having a good match with Appendix O conditions when a temperature correction factor is applied to the formulation. Additionally, results show an almost linear growth of roughness over the whole accretion time.

Nomenclature

A_c = accumulation parameter

A_i = area of a mesh triangular element, m^2

$A_{p,i}$ = projected area of a mesh triangular element, m^2

*PhD Student, Institute of Fluid Mechanics, Hermann-Blenk-Straße 37, 38108, Braunschweig, Germany.
†Research Engineer, PhD, ONERA DMPE, 2 avenue Edouard Belin, 31055 Toulouse, France.
‡PhD Student, Department of Aerospace Science and Technology, Via La Masa 34, 20156 Milan, Italy, AIAA University Student.
§Full Professor, Department of Aerospace Science and Technology, Via La Masa 34, 20156 Milan, Italy.
¶Head of Multiphase Flows & Icing Workgroup, Institute of Fluid Mechanics, Hermann-Blenk-Straße 37, 38108, Braunschweig, Germany.

A_p = area of discretized region, m^2

AOA = angle of attack, $^\circ$

C_t = Roughness correlation coefficient

c = chord length, m

D_r = average drag ratio

f_0 = freezing fraction at the stagnation point

h = height of the ice geometry measured from a reference geometry, m

h_{mean} = local mean height of the ice geometry, m

$\widetilde{h}_{mean}$ = modified local mean height of the ice geometry, m

I_τ = temporal term

K = proportionality factor

K_0 = modified inertia parameter

K_I = inertia parameter

K_T = temperature correction factor

k_s = local equivalent sand-grain roughness height, m

k_s^+ = roughness characteristic number

k_{sc}^+ = fully-rough regime limit

LWC_∞ = liquid water content of the cloud, $kg\,m^{-3}$

M = Number of discretized regions (analysis window) on the reference geometry

Ma = Mach number

MVD = median volume diameter of droplet-size distribution, m

N = Number of experimental points (centroids) in the analysis window

R_a = local average roughness of the ice geometry, m

R_q = local root-mean-square roughness of the ice geometry, m

$\widetilde{R_q}$ = modified local root-mean-square roughness of the ice geometry, m

R_q' = spatial component of McClain's model for the local root-mean-square roughness of the ice geometry, m

Re_c = Reynolds number based on c

Re_d = Reynolds number based on d_p

r_0 = radius of curvature of the leading edge, m

Sk = local skewness of the height of the ice geometry

$\widetilde{Sk}$ = modified local skewness of the height of the ice geometry

s = curvilinear distance

T_∞ = static temperature, K

t_{ice} = accretion time, s

U_∞ = airflow velocity, m s^{-1}

Wei = Weibull probability density function

$\mathbf{x}$ = Spatial location, m

β = collection efficiency

β_0 = collection efficiency at the stagnation point

β_{fb} = collection efficiency at liquid-film breakdown location

γ_s = angle between the local surface normal with the leading edge normal, °

ΔT_{0S} = difference of freezing temp. and the freestream total temp.

Δs = curvilinear size of discretized region, m

μ = dynamic viscosity of air, Pa s

ν = kinematic viscosity of air, m^2 s

ρ = density of air, kg m^{-3}

ρ_i = density of ice, kg m^{-3}

ρ_w = density of water, kg m^{-3}

τ_w = skin friction, N m^{-2}

I. Introduction

An aircraft exposed to icing conditions during atmospheric flight will be subjected to ice accretion over its components. Generally, the accreted ice presents a surface with different roughness levels which depend on the icing conditions. This ice roughness has a major impact on the growth rate of the ice shape due to its effect on the boundary layer properties such as the convective heat transfer [1].

The simulation of in-flight ice accretion via numerical tools generally consists of a quasi-steady process in which the various physics involved are successively resolved [2–10]. First, the thermo-aerodynamic flow around an object is calculated. Then, the trajectories and deposition of the water droplets are simulated. Finally, a thermodynamic balance is made on the surface to calculate local ice accretion rates, from which the ice shape is obtained. To quantify the influence of roughness during the thermo-aerodynamic calculation, an equivalent sand grain roughness height k_s is generally used both for RANS [11–13] and integral boundary layer methods [14, 15], although alternative approaches are under development [16, 17].

For the prediction of k_s, some authors [18, 19] have established some calculation methods. However, the determination of this parameter is still largely empirical. For instance, models of uniform k_s (constant in space and time)

have been developed through reverse engineering by authors like Ruff and Berkowitz [20], Shin and Bond [21] or Hedde and Guffond [22]. Like the model used in LEWICE [3], k_s is often related to the chord length c, as shown in equation (1). The proportionality factor K may depend on several global parameters related to icing conditions such as the liquid water content LWC_∞ of the icing cloud, the median volume diameter MVD of the droplet-size distribution of the icing cloud, the freestream temperature T_∞, the freestream velocity U_∞, and the freezing fraction at the stagnation point f_0.

$$k_s(\mathbf{x}, t_{ice}) = K\, c \tag{1}$$

Although these models are of great practical use, the theoretical basis on which they have been developed is rather weak. For example, the scaling by c has no justification other than practical. Moreover, these models can be based on curve fits made on dimensional quantities (e.g. LWC_∞ in $\mathrm{kg\,m^{-3}}$), posing difficulties for their generalization to conditions different from those from which the model was developed. In this perspective, the model used in ONICE2D, IGLOO2D [22] and especially in LEWICE [3] are considered appropriate since K is either constant ($K = 10^{-3}$ [22]) or based on f_0 ($K = 5 \cdot 10^{-4}\sqrt{0.15 + 0.3/f_0}$ [3]), which is one of the main non-dimensional parameters identified by Anderson [23, 24] for ice accretion modeling.

Nevertheless, these uniform roughness height models do not respect the observations made in many experimental works [25–30], which state that the roughness is not uniform on the whole ice surface and that it evolves with time. Regarding the spatial evolution on an airfoil, it is common to distinguish a low-roughness area near the stagnation point termed "smooth zone" [25, 26, 29, 30], "stagnation region" or "glaze-ice-plateau region" [28], where the roughness size is driven by the runback water. A region further downstream where the roughness size greatly increases is termed "rough zone" [25–27, 29, 30] or "collection region" [28], on which the roughness size is driven by water droplet impingement. Regarding the evolution over time, observations of Anderson [24] indicate that the roughness size increases during the first moments of accretion and then stabilizes. Some semi-empirical models of the roughness height evolution were proposed by McClain et al. [28, 31] and Han & Palacios [32]. These models are based in part on f_0 and the accumulation parameter A_c, being this discussed in more detail in section II.

The current study focuses on the analysis of the ice roughness in conditions representative of in-flight ice accretion, to support the further development of roughness size models. The ice shapes are generated on the Icing Wind Tunnel of the Technical University of Braunschweig (BIWT) [33], using a non-symmetrical airfoil as a test subject. The technique employed for the digitization of the ice shapes is based on photogrammetry [34], which is known to have been applied in the study of Hann [35] and validated in the study of Baghel et al. [36], both for icing applications. An analysis of the ice roughness is performed to obtain a spatial distribution of statistical parameters for various accretion times t_{ice}.

Regarding airfoils present in the literature of roughness-height studies, the most used airfoil is the NACA0012 [26–30]. Still, investigations have been done on non-symmetrical airfoils such as the HAARP-II profile [31, 37, 38], a NACA23012

profile [39] and a CRM65 swept wing [40]. The present study investigates ice accretion on a non-symmetric airfoil as well. In addition, since a length scale must be defined to analyze or model the experiments, either in equation (1) (where the chord length c was chosen) or to define the accumulation parameter A_c (where the radius of curvature at the leading-edge r_0 was chosen), it seems important to use different ratios c/r_0 in the generated databases. The airfoil of the current study presents $c/r_0 \simeq 42$, while the NACA0012 airfoil presents $c/r_0 \simeq 63$ and the HAARP-II airfoil presents $c/r_0 \simeq 66$ (concerning this two airfoils studied in the literature in sufficient detail).

As presented in section III, the range of non-dimensional parameters A_c and f_0 cover a broad spectrum of icing conditions. For example, with a maximum value of $A_c = 0.64$ ($A_c < 0.48$ in McClain's works [28] for instance), the condition suggested by Anderson that the roughness size no longer evolves for $A_c > A_{clim}$ ($A_{clim} = 0.15$ [24] or 0.4 [27]) can be analyzed. Also, as done in the works by McClain et al. [28, 37, 38, 41–43], two types of droplet sizes corresponding to different Appendices of the icing certification procedure [44] were studied: the standard Appendix C conditions, corresponding to small droplets with MVD $\simeq 20\,\mu$m, and the Appendix O conditions, for which a significant part of the droplet cloud is constituted of supercooled large droplets (SLDs) likely to splash when impinging on the airfoil.

The main statistical parameters used to characterize the roughness are presented in section II. A reference model, proposed by McClain et al. [28] is presented as well in this section, which will be used to analyze the data generated in the current study and to comment on the main original observations corresponding to the studied conditions compared to literature conditions. The experimental setup and icing conditions will be presented in section III. Since the raw data generated by the experiments are mainly ice shapes, the post-processing tools employed to derive statistic parameters are described in section IV. Finally, section V is dedicated to the discussion and analysis of the results.

II. Parameters for the statistical analysis

In many convective heat transfer models used for modeling ice accretion, k_s is used to model ice roughness [12–14, 45, 46]. This quantity is however difficult to characterize experimentally because it corresponds to the thickness of a sandpaper-type roughness which would provide the same aerodynamic shear stress τ_w as the geometrical roughness measured experimentally. In other words, k_s is a thickness that must be provided to the models to obtain the correct value of the skin friction, being not strictly a pure geometrical parameter. Many models relating k_s to geometrical parameters have therefore been developed. Some of these correlations are based on easily identifiable parameters for academic rough elements (hemispheres, cones), which do not properly represent the complex rough geometry found on iced surfaces. Therefore, for surfaces covered with rough elements of any shape, models based on the moments of the surface statistics seem to be the most promising. For example, in the model of Flack and Schultz [47] presented in equation (2), k_s is a function of the local value of the root mean square (RMS) R_q and the skewness Sk of the rough-surface probability density function.

$$k_s = 4.43 R_q \left(1 + Sk\right)^{1.37} \tag{2}$$

This formula has limitations. For example, it is only valid for the fully-rough regime, characterized by large roughness heights where $k_s^+ > k_{sc}^+$, with $k_s^+ = k_s\sqrt{\tau_w/\rho}/\nu$ and k_{sc}^+ presenting values on order of a few tens (for example, $k_{sc}^+ = 68$ after Nikuradse [48]), and for which the roughness effect is independent of the Reynolds number. Equation (2) also stands for $Sk > -1$, i.e. if the surface does not have too large troughs compared to peaks. Moreover, the rough elements must be densely distributed. Despite these limitations, this model could be used by Aupoix and Chedevergne boundary layer models [12, 46]. Among the moments of the surface statistics presented in the next section, R_q is therefore an important parameter.

A. Main statistical parameters of the rough iced surfaces

Let h_i be the local height of a point on the rough iced surface, compared to the clean airfoil surface. Then, it is possible to define the average height h_{mean} around this point from N neighboring points via equation (3). h_{mean} acts as well as the average ice thickness, which is related to the average shape of the ice deposit and can be used for the validation of ice accretion software.

$$h_{mean} = \frac{1}{N}\sum_{i=1}^{N} h_i \tag{3}$$

With this, different statistical parameters can be defined to characterize the rough surface, as presented by Thomas [49]. Although many parameters have been defined, the focus of the current study is on those that have been specifically characterized and modeled for iced surfaces.

The first statistic moment of the rough surface is the average roughness R_a defined in equation (4). This parameter was characterized and modeled by Han and Palacios [32, 50] in particular. The model they proposed is related to the accumulation parameter A_c, the freezing fraction at the stagnation point f_0, the chord length c, the radius of curvature at the leading edge r_0 and the local curvilinear abscissa.

$$R_a = \frac{1}{N}\sum_{i=1}^{N} \mid h_i - h_{mean} \mid \tag{4}$$

The second main parameter is the RMS of the roughness R_q, defined in equation (5), which is related to the second statistic moment. It is possible to link k_s to R_q as shown in equation (2). To do that, it is necessary to also characterize the skewness Sk as in equation (6) as well.

$$R_q = \left(\frac{1}{N}\sum_{i=1}^{N}(h_i - h_{mean})^2\right)^{0.5} \tag{5}$$

$$Sk = \frac{1}{NR_q^3} \sum_{i=1}^{N} (h_i - h_{mean})^3 \tag{6}$$

From here, it can be seen that R_q is thus important to characterize. In particular, McClain et al. [28] proposed the model described in the following section for R_q, based mainly on global parameters of the icing conditions, especially A_c and r_0, and applied to NACA0012 airfoils. In a more recent article (2021), McClain et al. [31] derived another model for R_q, which is not discussed in detail here. The latter model is better suited to the use in a numerical code because R_q is linked to local parameters such as the values of pressure, freezing fraction, etc. In addition, a larger database was investigated to derive the model, including airfoils other than NACA0012, namely the HAARP-II airfoil. Also, a large range of freezing fractions $f_0 \in [0.15, 0.88]$ was investigated, while $f_0 \simeq 0.2$ in 2017. However, although this may seem paradoxical, the latter model is less suitable for the comparisons made against the data generated in the present article because simulations with ice accretion software are required before the use of the model, making the results dependent on the implemented numerical models. In addition, the resulting properties of these simulations (pressure, freezing fraction, etc.) must correspond closely to those that McClain would have obtained with LEWICE2D. It turned out that IGLOO2D [5] in particular does not produce exactly the same freezing fraction as LEWICE2D (the discrepancy locally exceeds 100%, even though the predicted freezing fractions are very similar at the stagnation point). The choice was thus to focus on the model derived in 2017 by McClain et al. [28].

B. 2017 McClain's model for R_q

McClain et al. [28] proposed a model for R_q in the "collection region", in which they decorrelated the spatial and temporal evolution laws as in equation (7).

$$R_q = I_\tau R'_q \tag{7}$$

The temporal term I_τ is defined as in equation (8), which is driven by A_c, defined in equation 9. In these expressions, U_∞ is the far-field airflow velocity, LWC_∞ is the liquid water content of the cloud of droplets, t_{ice} is the exposure time, ρ_i is the ice density ($917\,\mathrm{kg\,m^{-3}}$) r_0 is the radius of curvature at the leading edge of the airfoil and β_0 is the collection efficiency at the stagnation point. The C_t coefficient was set to $C_t = 0.5$ for the straight and swept wings tested [28].

$$I_\tau = C_t A_c \beta_0 (2r_0) \tag{8}$$

$$A_c = \frac{U_\infty \,\mathrm{LWC}_\infty \, t_{ice}}{\rho_i \, (2r_0)} \tag{9}$$

In this model, the roughness increases linearly over time, via A_c, with no time limitations on the growth. This is not supported by all the authors, especially Anderson [27] which, as explained earlier, states that roughness stops growing

when a value of A_{clim} is reached.

After the suggestion of a reviewer of the current manuscript, it was noted that equation (7) doesn't consider the effect of T_∞, which actually affects roughness formation via its influence on f_0. Therefore, following this suggestion, a temperature correction factor K_T was implemented in equation (7), resulting in equation (10), being K_T modeled as in equation (11), taken from McClain et al. [31]. Here, ΔT_{0S} is the difference between the freezing temperature and the freestream total temperature.

$$R_q = I_\tau R'_q K_T \tag{10}$$

$$K_T = 0.34 + \Delta T_{0S}^{2/3} e^{-\Delta T_{0S}/2.25} \tag{11}$$

The spatial evolution of the roughness height is driven by the collection efficiency β and modeled as in equation (12). Here, the Weibull probability density function Wei is used to match the specific spatial evolution of the roughness height, as in equation (13).

$$R'_q = \frac{\text{Wei}\left(\beta - 0.05, \beta_{fb} - 0.15, 3\right)}{3.09\text{Wei}\left(0.875(\beta_{fb} - 0.15), \beta_{fb} - 0.15, 3\right)} + \frac{0.05}{3.09}\left(1 - \tanh\left(10\left[\beta_{fb} - \beta\right]\right)\right) \tag{12}$$

$$\text{Wei}\left(x, \lambda, k\right) = \frac{k}{\lambda}\left(\frac{x}{\lambda}\right)^{k-1} e^{-(x/\lambda)^k} \tag{13}$$

β_{fb} is the collection efficiency at the liquid-film breakdown location, i.e. at the end of the "glaze-ice plateau". In references [28, 43], $\beta_{fb} = 0.45$. Regarding the collection efficiency at the stagnation point, the model was developed using Langmuir and Blodgett's approach to assess β_0 [51], being this defined in equation (14). The modified inertia parameter K_0 is presented in equation (15).

$$\beta_0 = \frac{1.4\left(K_0 - \frac{1}{8}\right)^{0.84}}{1 + 1.4\left(K_0 - \frac{1}{8}\right)^{0.84}} \tag{14}$$

$$K_0 = \frac{1}{8} + D_r\left(K_I - \frac{1}{8}\right) \tag{15}$$

The inertia parameter K_I is defined as $K_I = \rho_w d_p^2 U_\infty / 18\mu(2r_0)$, ρ_w is the water density, d_p is the droplet diameter (in practice, d_p = MVD is used) and μ is the dynamic viscosity of air. The average drag ratio D_r is presented in equation (16), where the Reynolds number is $Re_d = U_\infty d_p / \nu$.

$$D_r = \frac{1}{0.8388 + 0.001483 Re_d + 0.1847 Re_d^{0.5}} \tag{16}$$

A sine law assumption was also used by McClain et al.[28] to obtain a distribution of the collection efficiency, presented in equation (17). AOA is the angle of attack, γ_s is the angle between the normal to the surface and the line joining the leading edge of the airfoil to the trailing edge, at the local curvilinear abscissa s. It can be noted that McClain's model has been developed to take into account a sweep-angle effect. The test article considered in this work is a straight wing, therefore, no sweep angle is considered.

$$\beta = \beta_0 \cos\left(\mathrm{AOA} + \gamma_s\right) \tag{17}$$

The models (7) and (10) are thus mainly dependent on A_c, r_0 and a spatial evolution of the collection efficiency β. Several limitations to the models are highlighted by McClain [28]. First, this model was developed for the "collection region" only, where the roughness height is linked to the droplet collection. Second, the value assigned to C_t is not firmly established (some possible adaptations are proposed for C_t in [43]). Third, McClain points out that equation (7) was established for a reduced range of freezing fraction f_0, for symmetric NACA0012 wings with zero AOA. The database investigated in [28] indeed consists of NACA0012 airfoils with AOA = 0, $A_c = 0.348$ and f_0 in the range from 0.19 to 0.25. NACA0012 swept-wings with $f_0 = 0.19$ or 0.22 and A_c in the range from 0.03 to 0.484 were investigated with the same model in [43]. It must also be mentioned that McClain studied rather short accretion times, with A_c values from 0.061 to 0.408 [42], which may explain the fact that no limitation was identified to the model in terms of the range of A_c.

The location of the film breakdown is probably one of the major difficulties of the model because no specific model is proposed for β_{fb}. McClain warns that investigating different values of f_0 could affect β_{fb}, as well as C_t and the parameters of the Weibull function. It can be assumed that the investigation of different wing profiles or different angles of attack can lead to the same consequences. In addition, while Langmuir and Blodgett's formula (14) often produces rather accurate results, especially for symmetric 2D airfoils [23], it has to be mentioned that equation (17) can be considered questionable, especially if generalized to several types of airfoils.

Since the icing conditions and experimental apparatus are quite different between the databases studied by McClain et al. [28] and in the present study, the model (7) will be used in section V to evaluate its capabilities, and thus, establish a connection between the experimental results generated in the BIWT and those studied by McClain. It must be underlined that a recalibration of the model proposed by McClain was necessary: The variables β_{fb}, C_t, and the parameters of the Weibull functions could be changed, as authorized by McClain's observations. In particular, β_{fb} was adjusted for each test case here proposed to correctly identify the region of the glaze ice plateau. Details on the values used for each of the test cases will be presented in section V.

III. Generation and digitization of ice shapes

A. Setup of experiments

The ice accretion experiments were performed in the BIWT, which has a test section of 1.5 m length, with a cross-section of 0.5 m × 0.5 m. The setup involved the HMDI airfoil as the test subject installed in the middle of the test section at an AOA of 0°, as shown in figures 1 and 2. The term HMDI stands for "Hybrid Moveable DeIcing systems", which was a LuFo project (20Y1512G)* on which this specific airfoil was commissioned for the testing of anti-icing and de-icing systems developed by collaborators such as Airbus and DLR. The airfoil was later transferred to the ICE GENESIS project†. Its geometry‡ is based on a scaled section of the wing of the NASA Common Research Model and resembles a NACA 1414 airfoil. The airfoil has a chord length $c = 0.7$ m, a spanwise length of 0.5 m and a leading edge curvature radius $r_0 = 0.0163$ m. The blockage ratio of the setup is of 0.25 at the location of the maximum thickness of the airfoil.

Fig. 1 Installation of the HMDI airfoil in the wind tunnel test section.

B. Test matrix and icing parameters

The experiments were carried out at a wind speed of 40 m s^{-1} and a pressure of 1 bar at the test section, resulting in a Reynolds number $Re_c \approx 2 \cdot 10^6$ and $Ma \approx 0.12$. Although many icing conditions were tested for the ICE GENESIS project, table 1 is presented showing all the selected test points for the current study. As seen, temperatures of −8 °C and −12 °C and accretion times of 1.5 to 9 minutes are analyzed, as well as two sets of particle distributions corresponding to Appendix C and Appendix O conditions of the EASA airplane certification standards [44]. Appendix C cases also included tests at −5 and −16 °C, which although processed, were not included in the current study. Indeed, the case at −16 °C is purely rime ice accretion, therefore the roughness is very limited and the study of this condition is less interesting compared to glaze ice. On the other hand, the tests at −5 °C presented complicated ice shapes for which the

*LuFo: Federal Aeronautical Research Programme of the DLR (German Aerospace Center).

†ICE GENESIS project: www.ice-genesis.eu

‡To this date, the geometry of the HMDI airfoil is not publicly available. Access to the geometry can be gained via the AIIS (Austrian Institute for Icing Sciences) database: icing-database.eu

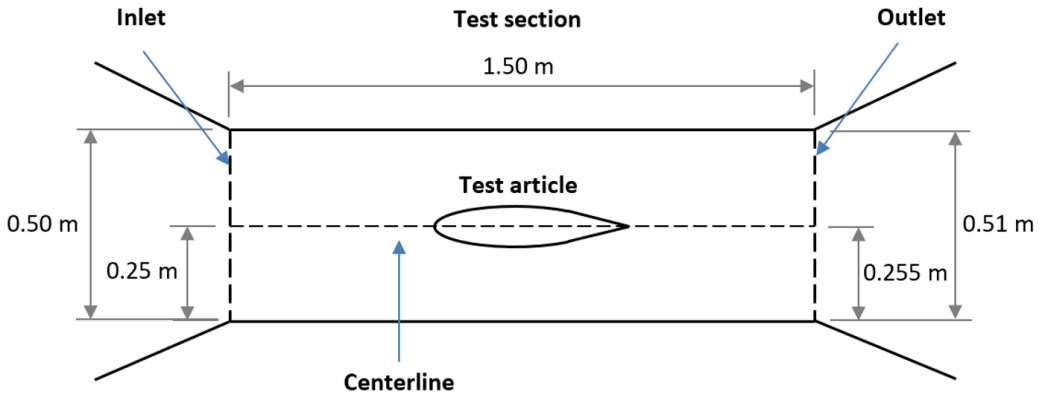

Fig. 2 Sketch of the installation of the HMDI airfoil in the wind tunnel test section.

convergence of the discrete statistical analysis is more complex to achieve, being this briefly in section IV.C.

Table 1 Icing conditions test matrix

Appendix	T_∞	t_{ice}	f_0	A_c
-	°C	min	-	-
C	-8	1.5 / 3 / 6 / 9	0.48	0.11 / 0.21 / 0.42 / 0.64
C	-12	1.5 / 3 / 6 / 9	0.71	0.11 / 0.21 / 0.42 / 0.64
O	-8	3 / 6 / 9	0.58	0.13 / 0.27 / 0.40
O	-12	3 / 6 / 9	0.85	0.13 / 0.27 / 0.40

Appendix C conditions involved a cloud with an MVD = 19 µm and $\text{LWC}_\infty = 0.88\,\text{g m}^{-3}$, while Appendix O conditions present an MVD = 70 µm and $\text{LWC}_\infty = 0.56\,\text{g m}^{-3}$. The particle distributions of the icing clouds are shown in figure 3. This allowed to cover icing conditions with a f_0 and A_c presented as well in table 1. As a note, f_0 is estimated following the procedure of Anderson [52] while A_c was calculated via equation (9). Information about the calibration of the droplet cloud and its uniformity can be found in the study of Knop et al. [53] for Appendix C, while the study of Bora et al. [54] presents information on the calibration of Appendix O.

C. Digitization via photogrammetry

The photogrammetry method consists in taking multiple pictures of an object from different angles (between 50 and 100 photos), which are then fed into a photogrammetry software that reconstructs a 3D model from the photos [34]. In the current study, the software 3DF Zephyr was employed[§]. More details on the validity and accuracy of the photogrammetry method applied to ice accretion are described in the study of Baghel et al. [36].

Therefore, once an ice shape was generated, the slat was taken to a cold chamber located near the test section in order to take the required photos using cameras Canon EOS 80D with a 55 mm lens. It is noted that the ice shape was

[§]3DF Zephyr: www.3dflow.net/3df-zephyr-photogrammetry-software

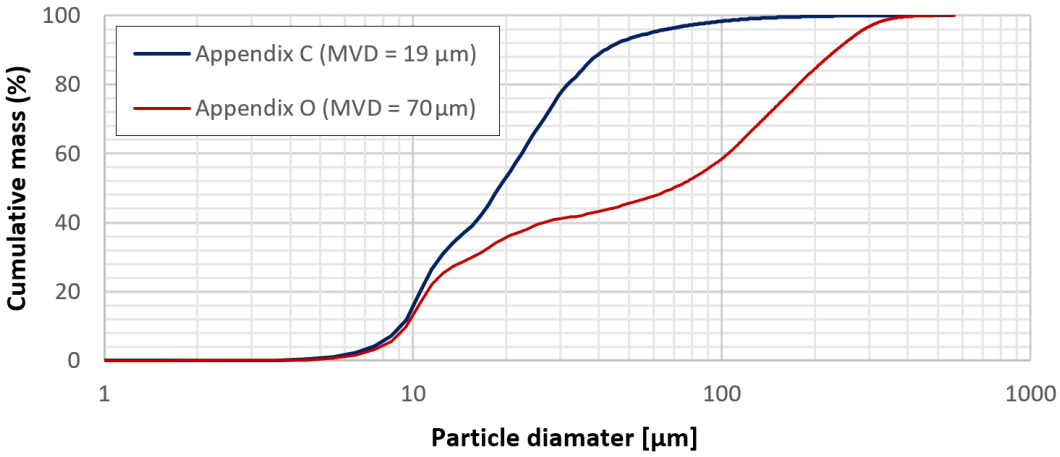

Fig. 3 Particle distributions of the icing clouds.

painted with a red ice marker in spray form to allow better resolution of the ice details, by suppressing natural ice reflections caused by its transparency and allowing for a better 3D model generation. An example of the taken photos of an ice shape and its corresponding 3D model can be seen in figure 4. Due to the nature of the process, the experimental ice shape is discarded afterward, meaning that each 3D model for each temperature and ice accretion time is made from independent experiments.

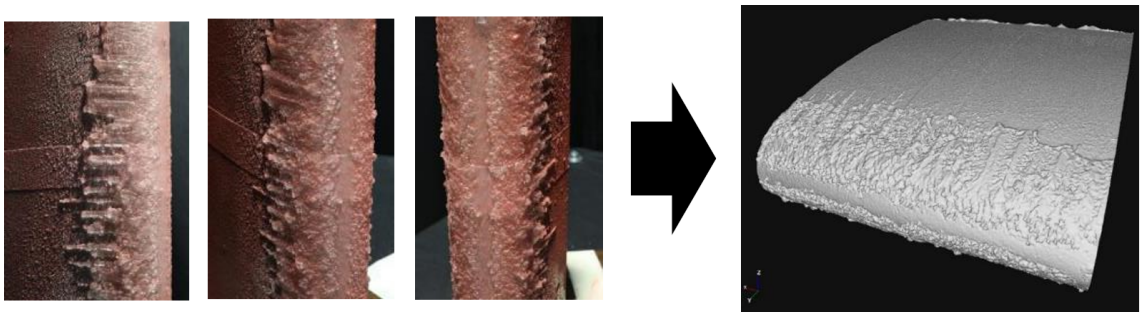

Fig. 4 Example of 3 photos from a set taken for an ice shape (left), used to generate a digital 3D model (right).

The reconstructed 3D ice model presents a span length of $\pm 50\,mm$ from the center. A proper alignment of the obtained 3D model with the slat of reference is performed using measured control points located on clean regions of the slat, which are captured as in the photos and set up in the software. The 3D ice model is a surface mesh made up of triangles (each triangle made by 3 nodes), stored as an STL file, which is used to perform the statistical analysis with the methods presented in the next section.

IV. Methods for statistical analysis

For the statistical analysis of the roughness of the experimental ice shapes presented in section III, three different methods are here presented and then compared to assess their validity.

A. Surface projection

The first two methods are based on the extraction of statistical parameters using a discretized reference geometry, which in this case is the slat of the 2D clean HMDI airfoil. Figure 5 shows an example of a 3D ice model of a digitized ice shape (app. O, −12°C and 9 min) being aligned with the HMDI airfoil, where the red dots correspond to the nodes of the surface mesh of the 3D ice model. Afterward, the 3D model is unwrapped following the unwrapping of the reference geometry from $x - y$ coordinates into $s - h$ coordinates, where s is the clean airfoil curvilinear abscissa and h is the normal distance of a node to the reference geometry, obtaining figure 6. The reference geometry will have $h = 0$ along the coordinate s.

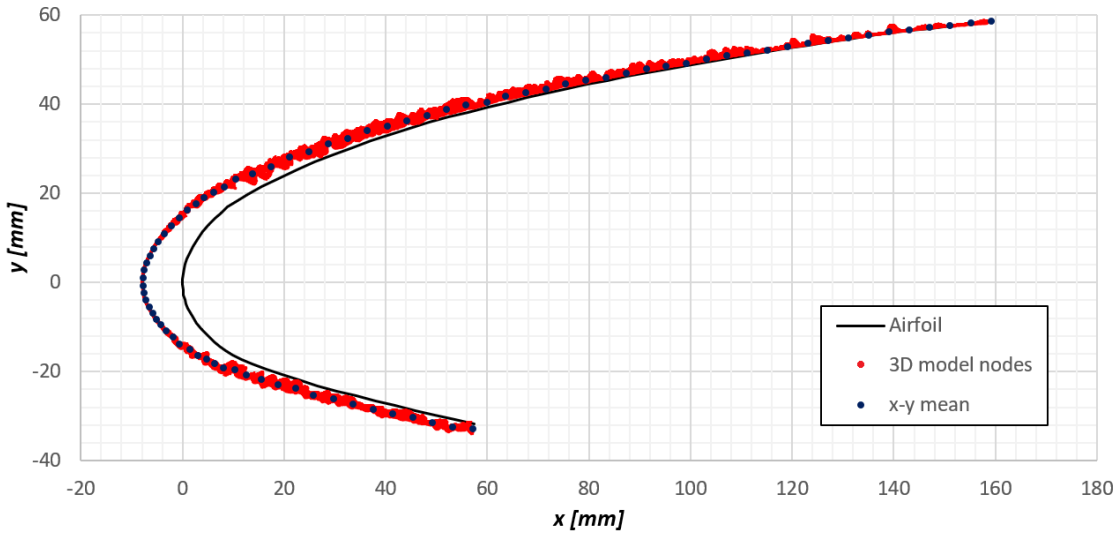

Fig. 5 HMDI airfoil and 3D ice model projected on the x-y plane.

For the extraction of statistical parameters, the first method uses equations (3), (5) and (6) to obtain h_{mean}, R_q and Sk at each analysis window j ($j \in [1, M]$, $M = 200$), which covers a range of $[s_j - \Delta s/2, s_j + \Delta s/2] \times [z_{min}, z_{max}]$, being $\Delta s = (s_{max} - s_{min})/M$. N is then the number of experimental points in the analysis window j. In these equations, h_i corresponds to the normal distance of the node i to the reference geometry. It can be said that the statistical parameters are based on the projection of the 3D model on the surface of the reference geometry, therefore it is termed as surface projection (SP) method. It is noted that Δs is chosen to be small enough to avoid curvature effects being added as roughness into R_q, while it is chosen as well to be big enough in order to still behave as a statistical parameter. Therefore, there is a range of values of Δs which don't have major effects on the obtained R_q distributions.

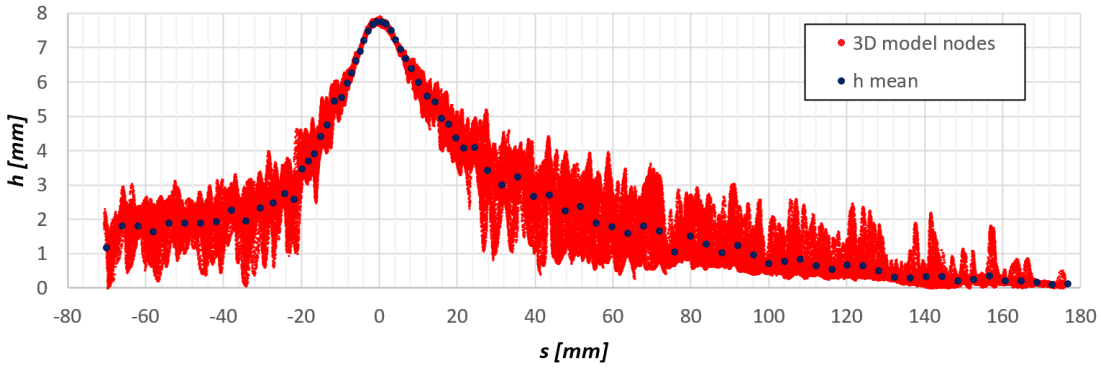

Fig. 6 Unwrapped 3D ice model on the s-h coordinate system based on the HMDI airfoil.

For the second method, these equations are modified into equations (18), (19) and (20). h_i would now correspond to the normal distance of the centroids of the mesh triangles to the reference geometry, while the $A_{p,i}$ is the projected area of the triangle on to the reference geometry and A_p is the sum of all these projected areas, as shown in figure 7. Since $A_{p,i}/A_p$ would act as a weight term over the original formulation, this method is termed as weighted surface projection (WSP) method. This modification is done to account for the different nodal densities of the ice shape, meaning that the SP and WSP methods would eventually give the same results for a mesh with a homogeneous distribution of elements.

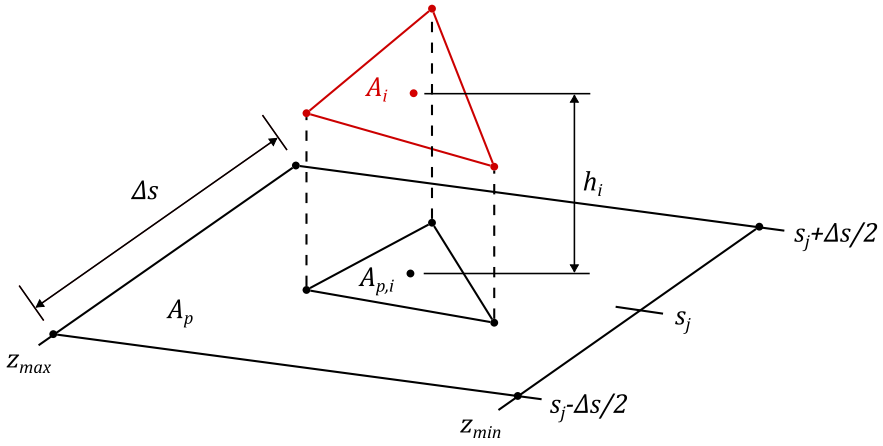

Fig. 7 Sketch of a mesh triangle and its projection on the reference geometry.

$$\widetilde{h}_{mean} = \frac{1}{N}\sum_{i=1}^{N}\frac{A_{p,i}}{A_p}h_i. \tag{18}$$

$$\widetilde{R_q} = \left(\frac{1}{N}\sum_{i=1}^{N}\frac{A_{p,i}}{A_p}(h_i - \widetilde{h}_{mean})^2\right)^{0.5} \tag{19}$$

$$\widetilde{Sk} = \frac{1}{N\widetilde{R_q}^3}\sum_{i=1}^{N}\frac{A_{p,i}}{A_p}(h_i - \widetilde{h}_{mean})^3 \tag{20}$$

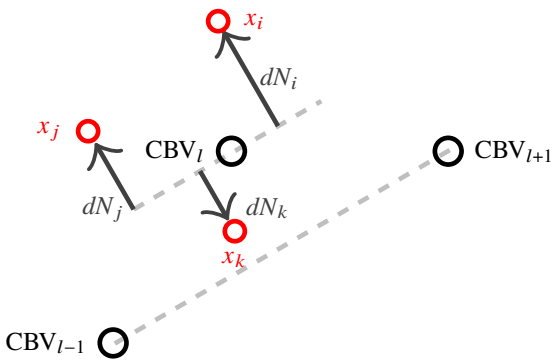

Fig. 8 Example of the normal distance between the data point and its best matching unit.

B. Self organizing maps

The third method is based on the self-organizing maps (SOM) approach, which is an unsupervised machine learning technique used to identify non-linear manifolds from a point cloud [39, 55–58], being this its main peculiarity compared to the other presented methods. Indeed, the SOM method is capable of dealing with non-functional structures like horns in glaze ice shape, when it is not possible to identify a one-to-one correspondence between the ice shape and a reference geometry such as the clean airfoil.

The scattered data is presented to the algorithm which reads the position of each mesh node. Then, a set of codebook vectors (CBV) is initialized. Following batch training, these CBVs are moved towards the centroid of a clump of clustered data, which will have that CBV as the best matching unit (BMU). At the end of the training, the result is a map of CBVs that represents the mean shape identified by the point cloud. In contrast to online training, where one random data point is used to update the CBVs position at each iteration, the update procedure of the batch training is done by considering the entire dataset. Therefore, the results of online training depend on the sequence of training data presented to the CBV, while results of batch training are guaranteed to be deterministic due to the usage of the same entire dataset [58]. During the training, the influence of each data point to a CBV is determined by a neighbourhood function. Points closer to the CBV will have a larger weight in updating the position of the CBV compared to points further away in the space. Different functions can be used for this purpose, such as the Gaussian function [58], which is used for the current study. The neighbourhood function introduces a radius of influence as a new parameter proper of the function. By reducing this radius, the region enclosing the training data point that influences the position of a CBV is reduced.

Finally, the last step consists on evaluating statistical parameters associated with the mean ice shape, that is, R_a and R_q. For each point of the clump, the normal distance $dN = h - h_{mean}$ from its BMU is computed. An example of the normal distance of each data of the cluster to its best matching unit is shown in Fig. 8. More details on this approach can be found in the work by McClain [39] and by Neubauer [56, 57].

To determine the number of CBVs and the neighbourhood function radius which guarantee consistent results, a

convergence analysis was performed. The number of CBVs was set to a minimum value that guaranteed not significant changes in the roughness profile when adding more CBVs. A similar procedure was followed for the radius of the neighbourhood function, which was decreased until significant changes on the mean shape or roughness were observed. For the test cases of the current study, the number of CBVs was set to 250 and the radius was set to 0.1.

C. Comparison of methods

A comparison of the extracted statistical parameters using the presented methods is shown at next. Figures 9 and 10 show the computed mean ice shape on the left, while R_q is shown on the right, for a case from Appendix C (−12°C, 3 min) and another of Appendix O (−8°C, 6 min), respectively. The SOM method does not need a reference geometry to determine the mean shape and roughness. Therefore, to compare its results with the other methods and with the empirical correlation, the CBVs must be projected on the clean airfoil surface. The discretization of the clean airfoil must be sufficiently fine to guarantee that each CBV is associated to one point on the clean airfoil.

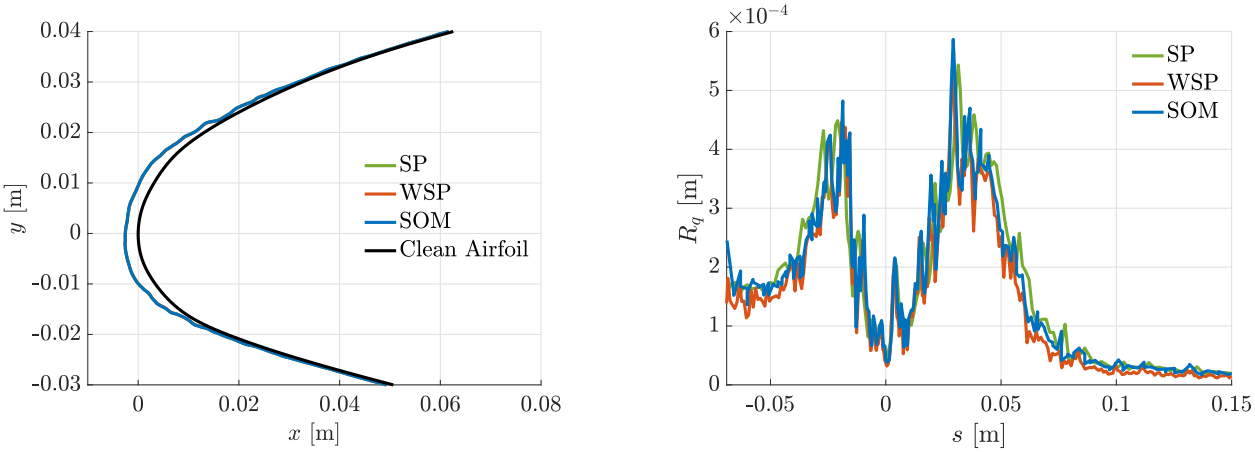

Fig. 9 Comparison of methods for the Appendix C case at −12°C, 3 min.

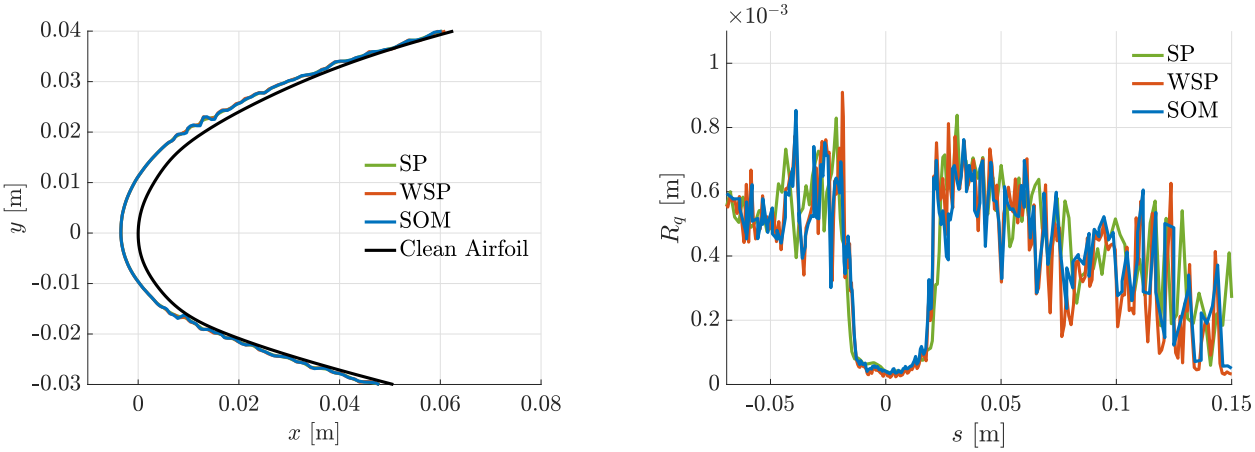

Fig. 10 Comparison of methods for the Appendix O case at −8°C, 6 min.

Regarding the mean ice shape, all three methods give almost perfectly overlapping results. Regarding R_q, this is shown against the clean airfoil curvilinear abscissa with $s = 0$ representing the leading edge, $s > 0$ being the suction side and $s < 0$ being the pressure side of the airfoil. The overall roughness trend is similarly captured by all methods both for Appendix C and Appendix O test cases. It can be seen that all methods can capture the low level of roughness around the stagnation point and also the peaks identified in the Appendix C test case. Overall it can be stated that the three methods are equivalent for the characterization of roughness. Therefore, in section V results obtained with the self-organizing maps approach will be presented.

Finally, as explained in section III.B, the tests at $T = -5\,^{\circ}\mathrm{C}$ were excluded from the analysis since the resultant ice shape presented complex features, as can be noticed from experimental data in Figure 11. One of the main concerns is to discriminate between what is to be considered as a geometrical feature of the ice shape and what is to be considered roughness. Indeed, as can be seen in Figure 11, where a horn is forming around $s = 0.04\,\mathrm{m}$ and $s = -0.03\,\mathrm{m}$, two possible interpretations arise. The first one, the orange curve i.e. Case 1, is to consider the average thickness as the mean shape, and everything else is considered as roughness. On the other hand, another possibility, shown with the blue curve i.e. Case 2, is that the horn is treated as a geometrical feature and the mean shape follows the horn, and the roughness is then evaluated from this mean shape. The two different shapes have been identified using the SOM approach with the same number of codebook vectors and two different radius: 0.1 for Case 1 and 0.03 for Case 2. This difference was not found in the other test cases with more regular ice shapes and using the values of radius above would give the same results in terms of mean shape and roughness. For this particular test case, a further detailed analysis on which of the two configuration obtained with SOM better represents reality and when convergence is considered to be reached should be conducted. Nevertheless, this analysis results in a complex problem out of the scope of the present work.

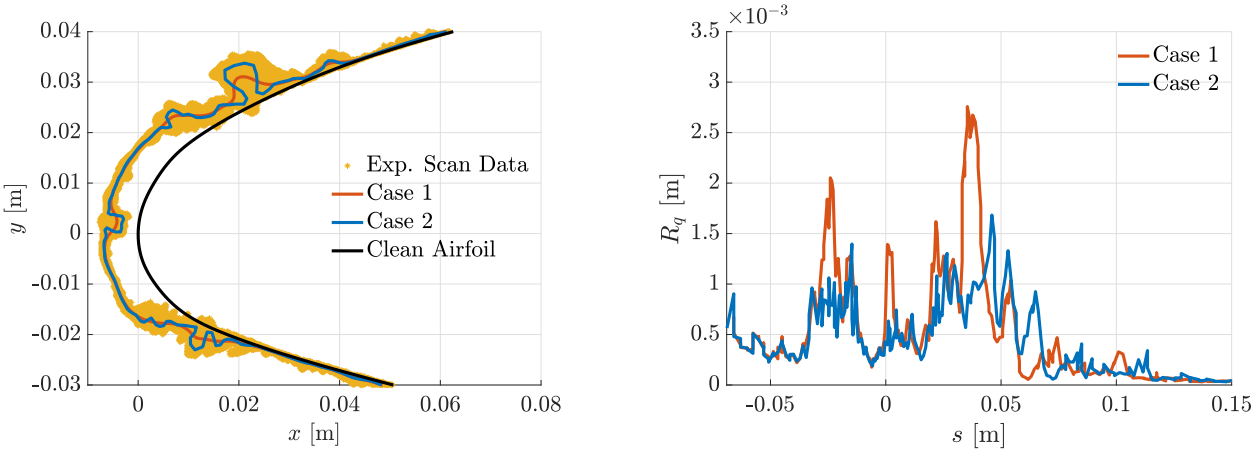

Fig. 11 Mean ice shape and R_q of Appendix C cases at $-5°$C.

V. Analysis and results

A. Appendix C

Figure 12 shows the extracted mean ice shape evolution over time for −8 and −12°C. A difference in the topology of the ice can be appreciated, especially at high accretion times. Development of horns can be seen for cases at −8°C.

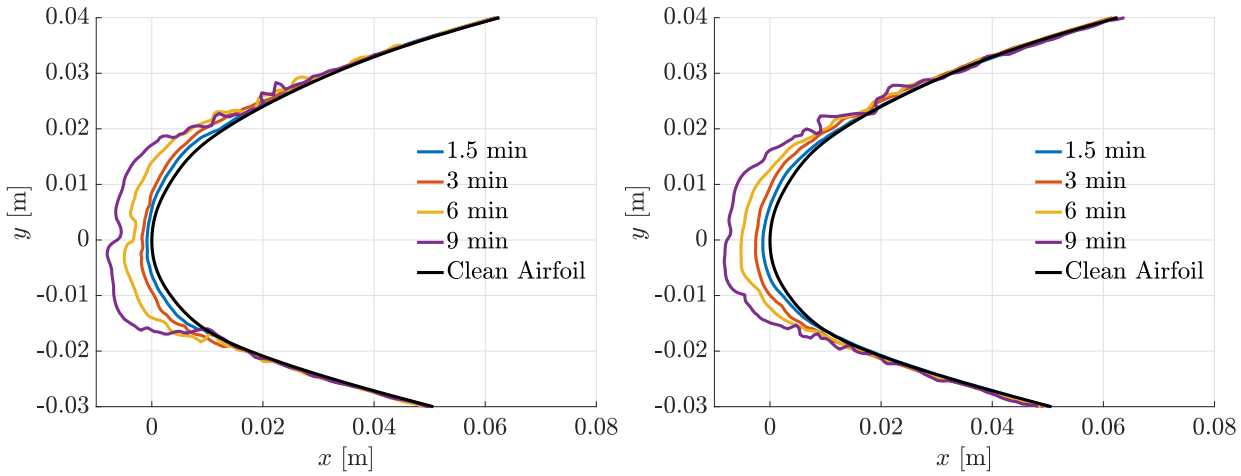

Fig. 12 Mean ice shape of Appendix C cases at −8°C and −12°C.

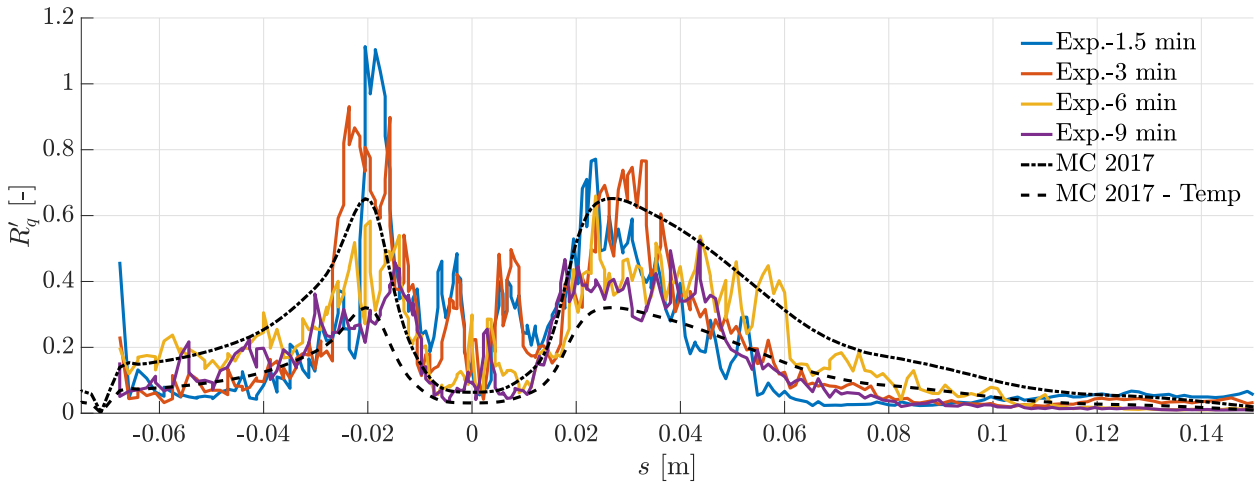

Fig. 13 R'_q for Appendix C cases at −8°C.

In order to simplify the analysis of R_q over time, the values of non-dimensionalized R'_q are presented in figures 13 and 14 (see equation (7)). This is based on the hypothesis that $R_q \propto t$, which is verified if R'_q is constant over t_{ice}. An increase of R'_q with t_{ice} implies a growth acceleration, while its decrease implies a deceleration.

As remarked in section II, a recalibration of the model was required in order to get the best fit of the roughness distribution. In particular, for Appendix C, the collection efficiency value at the end of the glaze ice plateau was $\beta_{fb} = 0.37$ for the test cases at −8°C and $\beta_{fb} = 0.36$ for the ones at −12°C. There is thus a small difference between

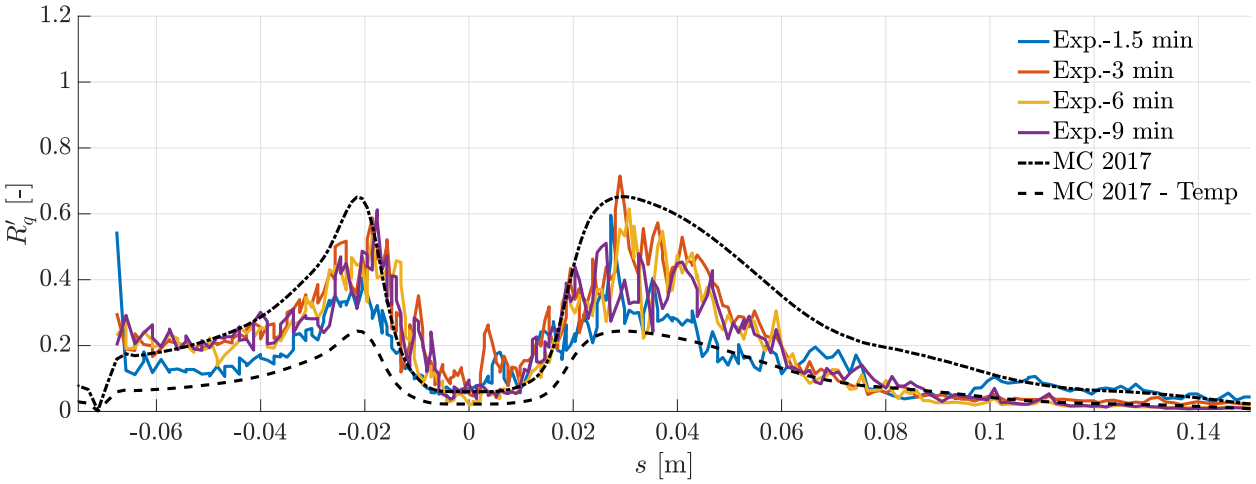

Fig. 14 R'_q for Appendix C cases at $-12\,^{\circ}$C.

the β_{fb} values for two very different values of f_0. This may indicate that the adjustment of β_{fb} compared to the value provided in the original model is related to the chosen airfoil. The time evolution does not change the plateau, therefore, the β_{fb} was kept constant while changing the ice accretion time, which is consistent with the model. Both cases indicate a good match between the extracted R'_q and McClain's proposed R'_q model (equation (12), dashed lines in figures 13 and 14), especially when observing the extent of the smooth zone and the overall evolution of R'_q in the collection region.

The cases at -8°C (figure 13) show an almost constant growth rate of R_q over time up to 9 minutes, indicated by the fact that all experimental R'_q curves overlap. Still, cases at -12°C (figure 14) exhibit a slight acceleration of the R_q growth rate in comparison to cases of -8°C (figure 13) . Nevertheless, the current tests didn't manage to show a strong growth deceleration of R_q, making it not possible to identify a threshold for A_c for which the roughness stops growing, at least for the range of A_c tested, which reaches the value of 0.64.

The temperature correction proposed in equation (10) is reported in figures 13 and 14 as well with a dashed line. It can be noticed that the proposed temperature correction does not improve the agreement with experimental data compared to the original model for Appendix C cases. Indeed, it generally underestimates the R'_q after the plateau region. Still, the experimental curves are enclosed between the original and temperature-corrected model, meaning that the two empirical models could represent the upper and lower bound of geometrical ice roughness.

As an observation, the experimental data seems to have a contaminated smooth zone, which can be appreciated in figure 15: some isolated ice elements randomly invade the smooth region. This situation has been also observed by McClain [41], attributing this effect to the airfoil size, with airfoils with a larger c presenting a cleaner and well-defined smooth zone.

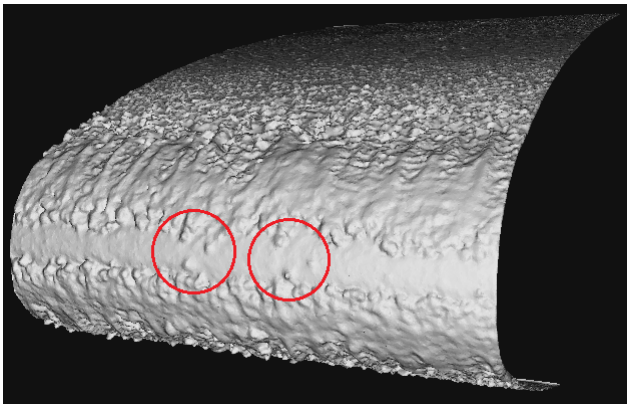

Fig. 15 3D model of a case at −8°C and 3 min of Appendix C. Invasive ice elements are highlighted in the smooth zone.

B. Appendix O

Figure 16 shows the mean ice shape evolution for −8 and −12°C. All ice shapes exhibit similar topology: A well-defined smooth zone, followed by a rough zone, with no presence of horns. It can be clearly seen that the ice thickness for cases at −12°C is higher around the stagnation point than for cases at −8°C, as expected. Following the same considerations taken on the analysis of Appendix C, figures 17 and 18 are presented. In particular, $\beta_{fb} = 0.52$ is selected for the test cases at −8°C and $\beta_{fb} = 0.56$ for the ones at −12°C. Also for Appendix O, these values were kept constant while changing the ice accretion time.

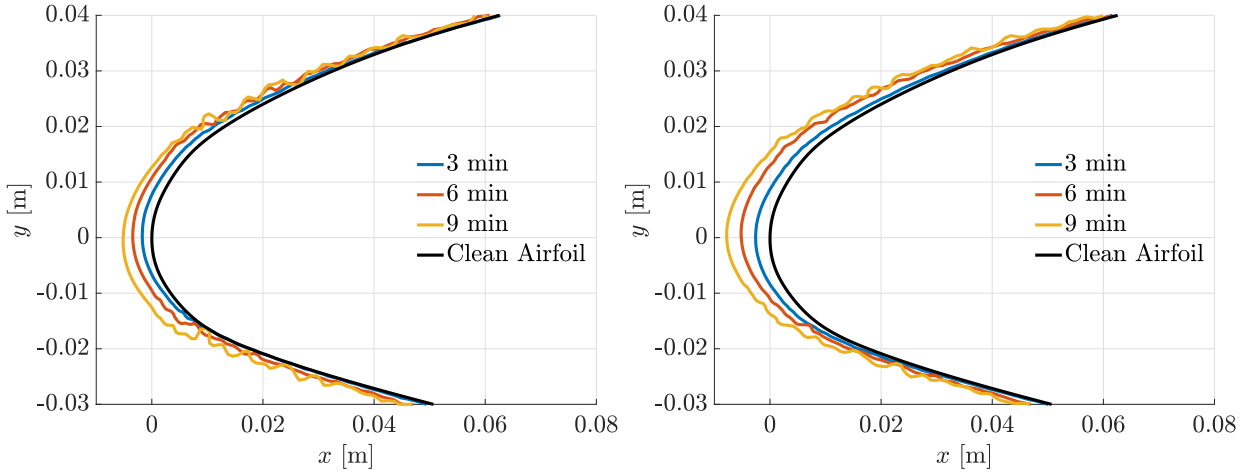

Fig. 16 Mean ice shape of Appendix O cases at −8°C and −12°C.

The values of R'_q show in evidence a wide smooth zone that follows McClain's proposed model until the sudden increase of R'_q on the rough zone, which then stays almost homogeneous over the rest of the ice shape. It can be seen that McClain's original model fails to predict the values R'_q for the rough zone. Still, McClain's corrected model (equation (10)) presents a better agreement with the experimental data. It can be seen that, as with the Appendix C cases, the two

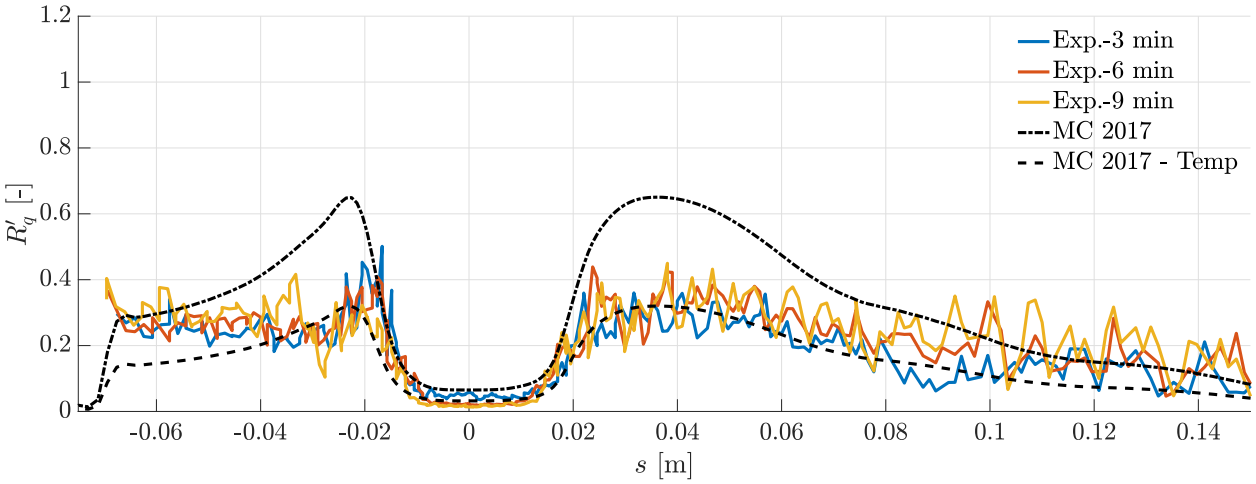

Fig. 17 R'_q for Appendix O cases at −8°C.

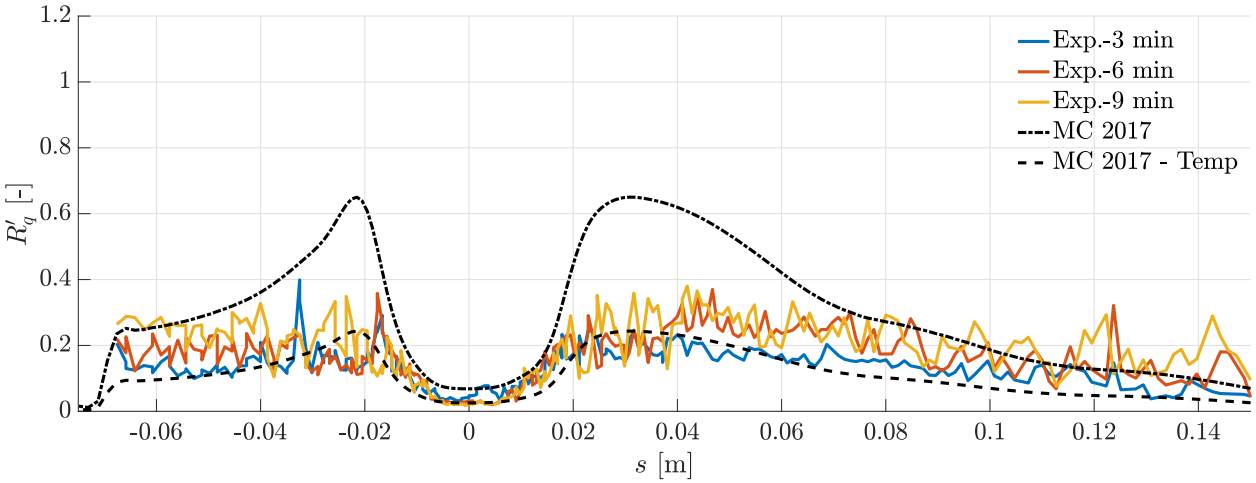

Fig. 18 R'_q for Appendix O cases at −12°C.

models bound the experimental data of Appendix O. This shows that the presented database is in agreement with other results from literature, from which the presented empirical models were elaborated. Nevertheless, further studies should be conducted on the range of applicability of these correlations.

Additionally, it can be stated that the growth of R'_q seems to be linear for $A_c < 0.4$ and no deceleration of the growth rate is observed, since all curves almost overlap, meaning that the maximum threshold of R'_q can't be identified.

Finally, in contrast to Appendix C cases, the present Appendix O cases don't exhibit major contamination or invasive rough elements on the smooth region, as can be seen in figure 19.

C. Notes on comparison between Appendix C and O cases

Comparison of the R_q values with cases with different MVD can be inaccurate due to some issues with the calculation of the collection efficiency. In the model proposed by McClain [28], the evaluation of the collection efficiency is

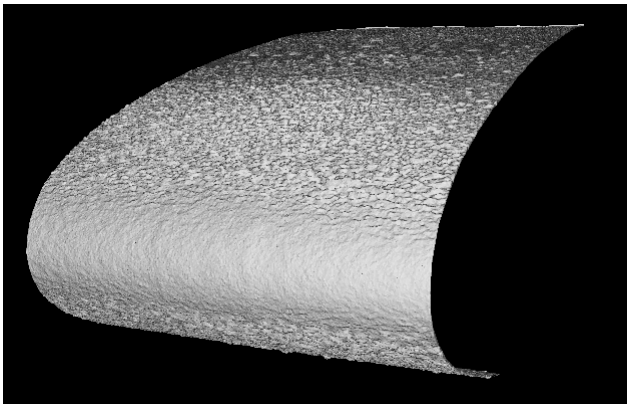

Fig. 19 3D model of case at −8°C and 3 min of Appendix O. The smooth zone seems free of invasive rough elements.

performed through the Langmuir and Blodgett's approach [51] presented in equation (14) considering only the MVD of the droplet cloud, obtaining the value $\beta_{0,\mathrm{MVD}}$ for Appendix C and O, shown in table 2.

By considering a multi-bin distribution on the Langmuir and Blodgett's approach for a more accurate calculation, different values of $\beta_{0,\mathrm{Bins}}$ are obtained, being shown in table 2. The Langmuir and Blodgett model, therefore, provides a rather close approximation of β_0 for Appendix C using the MVD, while this not being the case for Appendix O.

Table 2 Collection efficiency from Appendix C and O

Appendix	$\beta_{0,\mathrm{MVD}}$	$\beta_{0,\mathrm{Bins}}$	$\beta^{\mathrm{FS}}_{0,\mathrm{Bins}}$	$\beta^{\mathrm{WT}}_{0,\mathrm{Bins}}$
C	0.46	0.45	0.51	0.54
O	0.84	0.66	0.69	0.71

Furthermore, numerical simulations of particle trajectories could give more accurate but different values of collection efficiency: Table 2 shows the values $\beta^{\mathrm{FS}}_{0,\mathrm{Bins}}$ and $\beta^{\mathrm{WT}}_{0,\mathrm{Bins}}$, corresponding to results obtained from simulations of the airfoil in freestream and wind tunnel conditions, respectively, using the software PoliDrop [59] and DICEPS [60]. This leads to higher collection efficiencies for Appendix C cases in the wind tunnel due to blockage effects. These calculations were performed without accounting splashing phenomena, which could give even more different collection efficiencies.

It is therefore still a question of which value of collection efficiency should be used for the proper normalization of R_q in order to compare cases with different MVD, that is, Appendix C with Appendix O cases. In our study, $\beta_{0,\mathrm{MVD}}$ was used since the reference model was originally calibrated using this value.

VI. Conclusions

The current study presented the ice roughness analysis of digitized ice shapes obtained in the BIWT during the ICE GENESIS project. The analyzed ice shapes followed icing conditions described in Appendix C and O of EASA airplane certification standards.

For the digitization of the generated ice shapes, the photogrammetry method was applied, which reconstructs a 3D model via photogrammetry software based on sets of photos taken from an object at different angles.

The digitized ice shapes were analyzed using several methods for the extraction of statistical parameters, such as the mean ice shape and the RMS of the ice geometry, R_q. It was verified that all applied methods give approximately the same values.

During the analysis of Appendix C, it was noted that the roughness grows almost in a linear manner over time, showing almost no growth deceleration for $A_c < 0.64$. This made it impossible to identify a roughness limit in our experiments. A good match can be seen when comparing the obtained data to the original roughness distribution model of McClain [28], although when applying a temperature correction to the model, the obtained distribution underestimates roughness levels. It is interesting to note that only the parameter β_{fb}, related to the extension of the smooth zone, had to be changed to fit our data, despite the differences in airfoil geometry and conditions at which the model was originally calibrated.

Appendix O cases also show a linear growth of roughness but present a different distribution than the one of Appendix C. Therefore, the original McClain's model fails to predict the roughness distribution. Nonetheless, the proposed temperature correction improves the agreement between the generated database and the correlation, showing that the discrepancies between the original model and the Appendix O database cannot be entirely attributed to the different envelopes considered. In addition to this, no roughness growth limit could be observed for $A_c < 0.4$.

VII. Acknowledgment

This study was performed inside the ICE GENESIS project. This project has received funding from the European Union's Horizon 2020 research and innovation programme under agreement No 824310. The authors acknowledge the contribution of an anonymous reviewer who suggested the implementation of a temperature correction factor in the roughness correlation analyzed in the current manuscript.

References

[1] Hansman, R., JR, Reehorst, A., and Sims, J., "Analysis of surface roughness generation in aircraft ice accretion," *30th Aerospace Sciences Meeting and Exhibit*, 1992, p. 298.

[2] Gent, R. W., Dart, N. P., and Cansdale, J. T., "Aircraft icing," *Philosophical Transactions of the Royal Society of London. Series A: Mathematical, Physical and Engineering Sciences*, Vol. 358, No. 1776, 2000, pp. 2873–2911. https://doi.org/10.1098/rsta.2000.0689.

[3] Wright, W., "User's Manual for LEWICE Version 3.2," Tech. rep., NASA Contractor Report 2008-214255, 2008.

[4] Saeed, F., Gouttebroze, S., and Paraschivoiu, I., "Modified CANICE for Improved Prediction of Airfoil Ice Accretion," *48th Annual CASI Conference*, 2001.

[5] Trontin, P., Kontogiannis, A., Blanchard, G., and Villedieu, P., "Description and assessment of the new ONERA 2D icing suite IGLOO2D," 9th AIAA Atmospheric and Space Environments Conference - AVIATION 2017 DENVER, USA, AIAA 2017-3417, 2017. https://doi.org/10.2514/6.2017-3417.

[6] Ozcer, I. A., Aliaga, C., Pueyo, A., Zhang, Y., Fouladi, H., Nilamdeen, S., Selvanayagam, J., and Shah, S., "Ansys - Bombardier 1st Ice Prediction Workshop Results," *AIAA AVIATION 2022 Forum*, 2022. https://doi.org/10.2514/6.2022-3311.

[7] Forsyth, P., and Szilder, K., "Application of the Morphogenetic Approach to 1st AIAA Ice Prediction Workshop Test Cases," *AIAA AVIATION 2022 Forum*, 2022. https://doi.org/10.2514/6.2022-3609.

[8] Capizzano, F., Catalano, P., Carozza, A., Cinquegrana, D., and Petrosino, F., "CIRA contribution to the first AIAA Ice Prediction Workshop," *AIAA AVIATION 2022 Forum*, 2022. https://doi.org/10.2514/6.2022-3400.

[9] Morelli, M., Bellosta, T., Donizetti, A., and Guardone, A., "Assessment of the PoliMIce toolkit from the 1st AIAA Ice Prediction Workshop," *AIAA AVIATION 2022 Forum*, 2022. https://doi.org/10.2514/6.2022-3307.

[10] Radenac, E., and Duchayne, Q., "IGLOO3D simulations of the 1st AIAA Ice-Prediction-Workshop database," *AIAA AVIATION 2022 Forum*, 2022. https://doi.org/10.2514/6.2022-3310.

[11] Wilcox, D. C., "Reassessment of the scale-determining equation for advanced turbulence models," *AIAA Journal*, Vol. 26, No. 11, 1988, pp. 1299–1310. https://doi.org/10.2514/3.10041.

[12] Aupoix, B., "Roughness Corrections for the $k-\omega$ Shear Stress Transport Model: Status and Proposals," *Journal of Fluids Engineering*, Vol. 137, 2015, p. 021202. https://doi.org/10.1115/1.4028122.

[13] Aupoix, B., "Improved Heat Transfer Predictions on Rough Surfaces," *International Journal of Heat and Fluid Flows*, Vol. 56, 2015, pp. 160–171. https://doi.org/10.1016/j.ijheatfluidflow.2015.07.007.

[14] Kays, W. M., and Crawford, M. E., *Convective heat and mass transfer*, McGraw-Hill, 1993.

[15] Radenac, E., Kontogiannis, A., Bayeux, C., and Villedieu, P., "An extended rough-wall model for an integral boundary layer model intended for ice accretion calculations," *2018 Atmospheric and Space Environments Conference*, 2018. https://doi.org/10.2514/6.2018-2858.

[16] Wright, W. B., Porter, C. E., Galloway, E. T., and Rigby, D. L., "GlennICE 2.1 Capabilities and Results," *AIAA AVIATION 2022 Forum*, 2022. https://doi.org/10.2514/6.2022-3309.

[17] Chedevergne, F., "Modeling rough walls from surface topography to double averaged Navier-Stokes computation," *Journal of Turbulence*, Vol. 24, No. 1-2, 2023, pp. 36–56. https://doi.org/10.1080/14685248.2023.2173760.

[18] Fortin, G., Ilinca, A., Laforte, J.-L., and Brandi, V., "New Roughness Computation Method and Geometric Accretion Model for Airfoil Icing," *Journal of Aircraft*, Vol. 41, No. 1, 2004, pp. 119–127. https://doi.org/10.2514/1.173.

[19] Croce, G., Candido, E. D., Habashi, W., Munzar, J., Aubé, M., Baruzzi, G., and Aliaga, C., "FENSAP-ICE: Analytical model for spatial and temporal evolution of in-flight icing roughness," *Journal of Aircraft*, Vol. 47, No. 4, 2010, pp. 1283–1289. https://doi.org/10.2514/1.47143.

[20] Ruff, G., and Berkowitz, B., "Users Manual for the NASA Ice Accretion Prediction Code (LEWICE)," Tech. rep., NASA Contractor Report 185129, 1990.

[21] Shin, J., and Bond, T., "Experimental and computational ice shapes and resulting drag increase for a NACA 0012 airfoil," 5th Symposium on Numerical and Physical Aspects of Aerodynamic Flows, Long Beach, CA, United States, 1992.

[22] Hedde, T., and Guffond, D., "ONERA three-dimensional icing model," *AIAA Journal*, Vol. 33, No. 6, 1995, pp. 1038–1045. https://doi.org/10.2514/3.12795.

[23] Anderson, D., "Manual of scaling methods," Contractor Report 2004-212875, NASA, 2004.

[24] Anderson, D., and Shin, J., "Characterization of ice roughness from simulated icing encounters," 35th AIAA Aerospace Sciences Meeting and Exhibit 1997 RENO, USA, AIAA-97-0052, 1997. https://doi.org/10.2514/6.1997-52.

[25] Hansman Jr, R., and Turnock, S., "Investigation of surface water behavior during glaze ice accretion," *Journal of Aircraft*, Vol. 26, No. 2, 1989, pp. 140–147. https://doi.org/10.2514/3.45735.

[26] Shin, J., "Characteristics of Surface Roughness Associated With Leading Edge Ice Accretion," 32nd AIAA Aerospace Sciences Meeting and Exhibit 1994 RENO, USA, AIAA-94-0799, 1994. https://doi.org/10.2514/6.1994-799.

[27] Anderson, D., Hentschel, D., and Ruff, G., "Measurement and correlation of ice accretion roughness," 36th AIAA Aerospace Sciences Meeting and Exhibit 1998 RENO, USA, AIAA-98-0486, 1998. https://doi.org/10.2514/6.1998-486.

[28] McClain, S., Vargas, M., Tsao, J.-C., Broeren, A., and Lee, S., "Ice accretion roughness measurements and modeling," 7th European Conference for Aeronautics and Space Sciences (EUCASS), EUCASS2017-555, 2017. https://doi.org/10.13009/EUCASS2017-555.

[29] Han, Y., and Palacios, J., "Transient heat transfer measurements of surface roughness due to ice accretion," 6th AIAA Atmospheric and Space Environments Conference - AVIATION 2014 ATLANTA, USA, AIAA 2014-2464, 2014. https://doi.org/10.2514/6.2014-2464.

[30] Bansmer, S., and Steiner, J., "Ice roughness and its impact on the ice accretion process," 8th AIAA Atmospheric and Space Environments Conference - AVIATION 2016 WASHINGTON, USA, AIAA 2016-3591, 2016. https://doi.org/10.2514/6.2016-3591.

[31] McClain, S. T., Vargas, M. M., Tsao, J.-C., and Broeren, A. P., "A Model for Ice Accretion Roughness Evolution and Spatial Variations," AIAA AVIATION 2021 FORUM, 2021. https://doi.org/10.2514/6.2021-2641.

[32] Han, Y., and Palacios, J., "Surface roughness and heat transfer improved predictions for aircraft ice-accretion modeling," *AIAA Journal*, Vol. 55, No. 4, 2017, pp. 1318–1331. https://doi.org/10.2514/1.J055217.

[33] Bansmer, S. E., Baumert, A., Sattler, S., Knop, I., Leroy, D., Schwarzenboeck, A., Jurkat-Witschas, T., Voigt, C., Pervier, H., and Esposito, B., "Design, construction and commissioning of the Braunschweig Icing Wind Tunnel," *Atmos. Meas. Tech.*, Vol. 11, 2018, pp. pp. 3221–3249.

[34] Dai, F., and Lu, M., "Assessing the accuracy of applying photogrammetry to take geometric measurements on building products," *Journal of construction engineering and management*, Vol. 136, No. 2, 2010, pp. 242–250.

[35] Hann, R., "UAV icing: Ice accretion experiments and validation," *SAE International*, 2019. https://doi.org/10.4271/2019-01-2037.

[36] Baghel, A. P., Sotomayor-Zakharov, D., Knop, I., and Ortwein, H.-P., "Detailed Study of Photogrammetry Technique as a Valid Ice Accretion Measurement Method," Tech. rep., SAE Technical Paper, 2023.

[37] McClain, S. T., Vargas, M. M., Tsao, J.-C., and Broeren, A. P., "Ice Roughness and Thickness Evolution on a Business Jet Airfoil," 2018 Atmospheric and Space Environments Conference, 2018. https://doi.org/10.2514/6.2018-3014.

[38] McClain, S. T., Vargas, M. M., Tsao, J.-C., and Broeren, A. P., "Influence of Airfoil Angle of Attack on Ice Accretion Roughness," AIAA AVIATION 2020 FORUM, 2020. https://doi.org/10.2514/6.2020-2807.

[39] McClain, S. T., and Kreeger, R. E., "Assessment of Ice Shape Roughness Using a Self-Organizing Map Approach," *5th AIAA Atmospheric and Space Environments Conference*, 2013, p. 2546.

[40] McClain, S. T., Vargas, M. M., Tsao, J.-C., and Broeren, A. P., "Ice Accretion Roughness Variations on a Hybrid CRM65-Midspan Wing Model," *AIAA AVIATION 2021 FORUM*, 2021. https://doi.org/10.2514/6.2021-2686.

[41] McClain, S., Vargas, M., and Tsao, J.-C., "Characterization of ice roughness variations in scaled glaze icing conditions," 8th AIAA Atmospheric and Space Environments Conference - AVIATION 2016 WASHINGTON DC, USA, AIAA 2016-3592, 2016. https://doi.org/10.2514/6.2016-3592.

[42] McClain, S., "Manual point cloud registration for combined ice roughness and ice thickness measurements," 8th AIAA Atmospheric and Space Environments Conference - AVIATION 2016 WASHINGTON DC, USA, AIAA 2016-3590, 2016. https://doi.org/10.2514/6.2016-3590.

[43] McClain, S., Vargas, M., and Tsao, J.-C., "Ice roughness and thickness evolution on a swept NACA0012 airfoil," 9th AIAA Atmospheric and Space Environments Conference - AVIATION 2017 DENVER, USA, AIAA 2017-3585, 2017. https://doi.org/10.2514/6.2017-3585.

[44] EASA, "Certification Specifications and Acceptable Means of Compliance for Large Aeroplanes," *C-25, Amendment 27*, 2022.

[45] Makkonen, L., "Heat transfer and icing of a rough cylinder," *Cold regions science and technology*, Vol. 10, No. 2, 1985, pp. 105–116. https://doi.org/10.1016/0165-232X(85)90022-9.

[46] Chedevergne, F., "Analytical wall function including roughness corrections," *International Journal of Heat and Fluid Flow*, Vol. 73, 2018, pp. 258–269. https://doi.org/https://doi.org/10.1016/j.ijheatfluidflow.2018.08.001.

[47] Flack, K. A., and Schultz, M. P., "Review of Hydraulic Roughness Scales in the Fully Rough Regime," *Journal of Fluids Engineering*, Vol. 132, No. 4, 2010. https://doi.org/10.1115/1.4001492.

[48] Nikuradse, J., *Laws of flow in rough pipes*, National Advisory Committee for Aeronautics Washington, Technical Memorandum 1292, 1950.

[49] Thomas, T., "Characterization of surface roughness," *Precision Engineering*, Vol. 3, No. 2, 1981, pp. 97–104. https://doi.org/https://doi.org/10.1016/0141-6359(81)90043-X.

[50] Han, Y., "Aerodynamics and thermal physics of helicopter ice accretion," Ph.D. thesis, The Pennsylvania State University, 2016.

[51] Langmuir, I., and Blodgett, K., "A Mathematical Investigation of Water Droplet Trajectories," Technical Report 5418, Army Air Forces, 1946.

[52] Anderson, D., "Methods for scaling icing test conditions," *33rd aerospace sciences meeting and exhibit*, 1995, p. 540.

[53] Knop, I., Bansmer, S. E., Hahn, V., and Voigt, C., "Comparison of different droplet measurement techniques in the Braunschweig Icing Wind Tunnel," *Atmospheric Measurement Techniques*, Vol. 14, No. 2, 2021, pp. 1761–1781.

[54] Bora, V. R., Knop, I., Lucke, J., and Jurkat-Witschas, T., "Instrumentation for Measuring Supercooled Large Droplet Cloud Distributions in Icing Wind Tunnels," *AIAA SCITECH 2023 Forum*, 2023, p. 2286.

[55] Gallia, M., Bellosta, T., and Guardone, A., "Automatic roughness characterization of simulated ice shapes," *Journal of Computational and Applied Mathematics*, 2023, p. 115114. https://doi.org/10.1016/j.cam.2023.115114.

[56] Neubauer, T., and Puffing, R., "Assessment of Ice Shape Roughness via Automatic Spacing of Codebook Vectors in a Two-Dimensional Self-Organizing Map," *AIAA AVIATION 2020 FORUM*, 2020, p. 2806.

[57] Neubauer, T., Hassler, W., and Puffing, R., "Ice Shape Roughness Assessment Based on a Three-Dimensional Self-Organizing Map Approach," *AIAA AVIATION 2020 FORUM*, 2020, p. 2805.

[58] Ponmalai, R., and Kamath, C., "Self-Organizing Maps and Their Applications to Data Analysis," 2019. https://doi.org/10.2172/1566795, URL https://www.osti.gov/biblio/1566795.

[59] Bellosta, T., Parma, G., and Guardone, A., "A Robust 3D Particle Tracking Solver of in-Flight Ice Accretion using, Arbitrary Precision Arithmetics," *VIII International Conference on Coupled Problems in Science and Engineering*, 2019.

[60] Sotomayor-Zakharov, D., Sobotta, B., and Knop, I., "A dynamic collection efficiency formulation implemented in the icing code DICEPS," *International Journal of Heat and Mass Transfer*, Vol. 217, 2023, p. 124590.